Report

Cell Reports

Cryo-EM structure of the entire FtsH-HflKC AAA protease complex

Graphical abstract

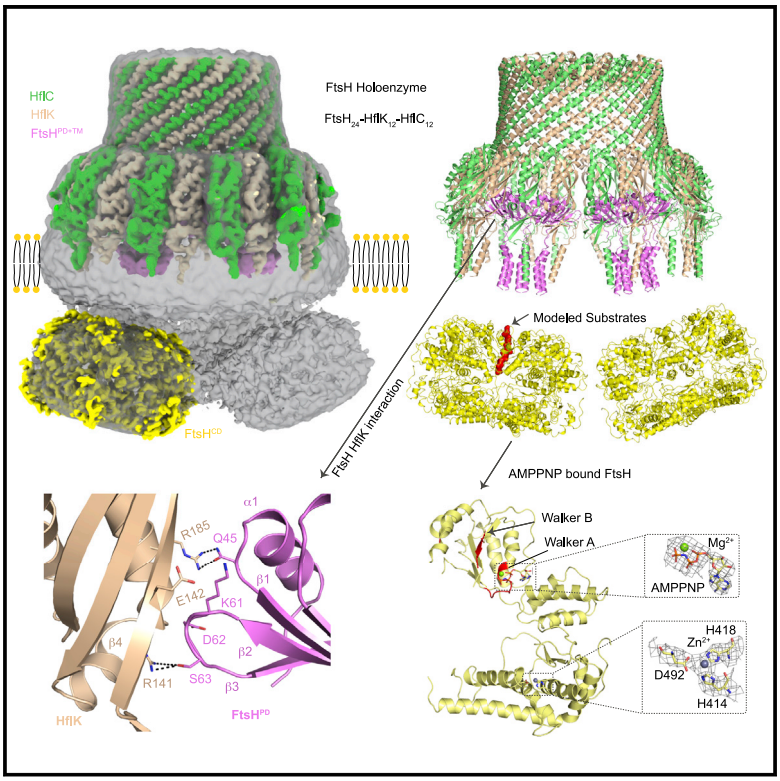

Highlights

- Cryo-EM structure of the entire FtsH-HflKC complex is solved
- 12 HflK and HflC interact with each other and encompass 4 FtsH hexamers
- HflK interacts with the FtsH β2-β3 loop to contribute to complex formation
- The cytoplasmic domain and the transmembrane helices of FtsH are featured

Authors

Zhu Qiao, Tatsuhiko Yokoyama, Xin-Fu Yan, ..., Sandip Basak, Yoshinori Akiyama, Yong-Gui Gao

Correspondence

yakiyama@infront.kyoto-u.ac.jp (Y.A.), ygao@ntu.edu.sg (Y.-G.G.)

In brief

Qiao et al. solved the *Escherichia coli* AAA protease FtsH together with its modulator HflKC complex, revealing that 12 HflK interact extensively and reciprocally with 12 HflC to encompass 4 FtsH hexamers through HflK and the FtsH β2-β3 loop.

Qiao et al., 2022, Cell Reports *39*, 110890
May 31, 2022
https://doi.org/10.1016/j.celrep.2022.110890

CellPress

Cell Reports

CellPress
OPEN ACCESS

Report

Cryo-EM structure of the entire FtsH-HflKC AAA protease complex

Zhu Qiao,[1,2] Tatsuhiko Yokoyama,[3] Xin-Fu Yan,[1,2] Ing Tsyr Beh,[1] Jian Shi,[4] Sandip Basak,[1] Yoshinori Akiyama,[3,*] and Yong-Gui Gao[1,2,5,*]

[1]School of Biological Sciences, Nanyang Technological University, Singapore 637551, Singapore
[2]NTU Institute of Structural Biology, Nanyang Technological University, Singapore 639798, Singapore
[3]Institute for Life and Medical Sciences, Kyoto University, Kyoto 606-8507, Japan
[4]Department of Biological Sciences, National University of Singapore, Singapore 117558, Singapore
[5]Lead contact
*Correspondence: yakiyama@infront.kyoto-u.ac.jp (Y.A.), ygao@ntu.edu.sg (Y.-G.G.)
https://doi.org/10.1016/j.celrep.2022.110890

SUMMARY

The membrane-bound AAA protease FtsH is the key player controlling protein quality in bacteria. Two single-pass membrane proteins, HflK and HflC, interact with FtsH to modulate its proteolytic activity. Here, we present structure of the entire FtsH-HflKC complex, comprising 12 copies of both HflK and HflC, all of which interact reciprocally to form a cage, as well as four FtsH hexamers with periplasmic domains and transmembrane helices enclosed inside the cage and cytoplasmic domains situated at the base of the cage. FtsH K61/D62/S63 in the β2-β3 loop in the periplasmic domain directly interact with HflK, contributing to complex formation. Pull-down and *in vivo* enzymatic activity assays validate the importance of the interacting interface for FtsH-HflKC complex formation. Structural comparison with the substrate-bound human m-AAA protease AFG3L2 offers implications for the HflKC cage in modulating substrate access to FtsH. Together, our findings provide a better understanding of FtsH-type AAA protease holoenzyme assembly and regulation.

INTRODUCTION

Given the crucial functions, large quantities, and complicated biogenesis processes of proteins, protein quality control is critically important for cell proteome homeostasis. Diverse chaperones and proteases have been reported to maintain protein quality control, including protein folding and assembly, as well as the degradation of misfolded, misassembled, aggregated, or dysfunctional proteins (Chen et al., 2011; Dalbey et al., 2012). FtsH, a unique essential membrane-bound ATP-dependent protease in *E coli*, is involved in the quality control of both membrane and nonmembrane proteins (Ito and Akiyama, 2005; Tomoyasu et al., 1995). *E. coli* FtsH has two inner-membrane transmembrane helices ($FtsH^{TM}$) with a periplasmic domain ($FtsH^{PD}$) at the N terminus and a cytoplasmic domain ($FtsH^{CD}$) containing both AAA ATPase and zinc protease domains at the C terminus (Figure S1A). Similar to a typical AAA ATPase domain, the domain in FtsH consists of universally conserved Walker motifs (A and B) and an arginine finger motif. The function of the C-terminal protease domain is to cleave unfolded proteins into short peptides with a metal ion (Zn^{2+}) acting as a cofactor coordinated by the HEXXH motif (Figure S1A) (Akiyama et al., 1996). FtsH-type AAA proteases are widely distributed in prokaryotic and eukaryotic cells, mainly in mitochondria and chloroplasts (Ito and Akiyama, 2005). Interestingly, two FtsH-type proteases, the i-AAA (intermembrane space) protease YMEL1 and the m-AAA (matrix) protease AFG3L2, are anchored to the mitochondrial inner membrane, with the protease domain facing the intermembrane space and the matrix, respectively (Puchades et al., 2017, 2019).

Given the functional significance of FtsH in protein quality control, its protease activity needs to be finely regulated. The HflKC protein complex has been proposed to function as a modulator that regulates the degradation of substrates (Kihara et al., 1996, 1998). Both HflK and HflC proteins, encoded by the two genes (*hflK* and *hflC*, respectively) that are located in one operon, consist of a single transmembrane helix at the N terminus, which is followed by a large periplasmic prohibitin homology (PHB) domain (Figure S1A). This PHB domain, belonging to the stomatin, prohibitin, flotillin, and HflKC (SPFH) domain family, has been found in various proteins and has been implicated in diverse functions (Brand et al., 2012; Chiba et al., 2006; Yokoyama et al., 2008). For instance, the prohibitin complex (PHB1 and PHB2), located in human mitochondria, has been reported to interact with the FtsH homolog AFG3L2 to negatively regulate its proteolytic activity and function as a membrane-embedded chaperone to enhance protein stabilization (Nijtmans et al., 2000; Tatsuta et al., 2005). So the prohibitin complex has been implicated in diverse functions, and its dysfunction is directly linked to diseases (Back et al., 2002; Nijtmans et al., 2002).

FtsH, HflK, and HflC are all membrane proteins, and the entire holoenzyme embodies an extremely large protein complex (Saikawa et al., 2004) . Most of the structural studies thus far have focused on the individual domains (periplasmic, ATPase, and

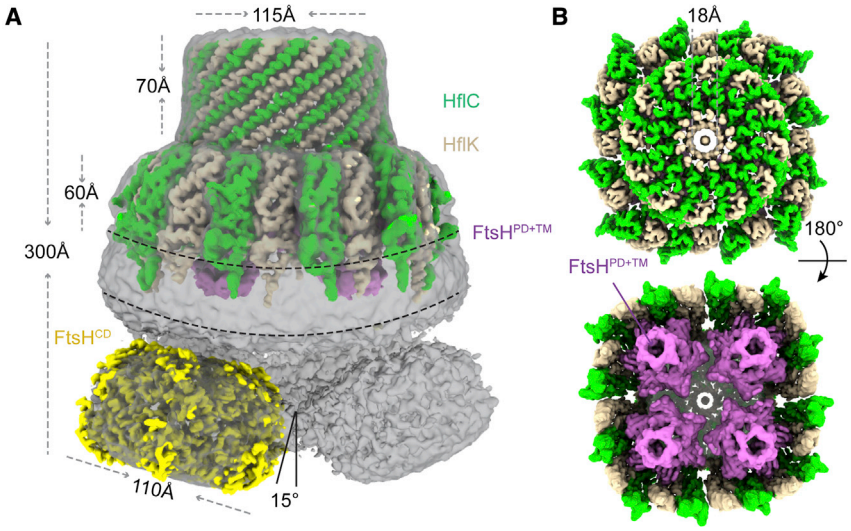

Figure 1. Cryo-EM map of the entire FtsH-HflKC complex

(A) Overall 3D-reconstructed map of the entire FtsH-HflKC complex. The isolated processed 3D-reconstructed map of $FtsH^{PD+TM}$-HflKC (wheat for HflK, lime for HflC, and violet for $FtsH^{PD+TM}$) and $FtsH^{CD}$ (yellow) were fitted to the overall FtsH-HflKC map (gray). The dimensions are shown in angstroms (Å), and the axis of the $FtsH^{CD}$ hexamer is tilted by 15° regarding the HflKC complex.

(B) The isolated $FtsH^{PD+TM}$-HflKC map is in the same color as shown in (A). The central pore of the cage cap (top view) and the four tunnels(bottom view), all of which are ~18 Å in diameter, are clearly visualized.

See also Figures S1–S3 and S10 and Table S1.

protease domains) or the entire FtsH cytosolic region (Bieniossek et al., 2006, 2009; Ito and Akiyama, 2005; Krzywda et al., 2002; Niwa et al., 2002; Scharfenberg et al., 2015; Suno et al., 2006, 2012; Vostrukhina et al., 2015). In particular, the structures of yeast i-AAA protease YME1 and human m-AAA protease AFG3L2 have provided molecular insights into the "spiral staircase" substrate translocation mechanism and many neurological phenotypes associated with AFG3L2 (Puchades et al., 2017, 2019). The cryoelectron microscopy (cryo-EM) structure of full-length FtsH from *Aquifex aeolicus* at a low resolution of ~12 Å revealed that the cytosolic domain is tilted regarding the transmembrane helices in the FtsH hexamer (Carvalho et al., 2021). However, detailed information about the FtsH-HflKC complex is still missing. To close the gap and to better understand the molecular mechanism of FtsH and FtsH-type proteases in protein quality control, the atomic structure of the entire FtsH-HflKC complex is urgently needed. While our manuscript was in preparation, another group reported the cryo-EM structure of FtsH-HflKC (Ma et al., 2022), which lacks the transmembrane helices and cytosolic domains for FtsH. Here, we report the cryo-EM structure of the entire FtsH-HflKC complex in combination with pull-down and *in vivo* enzyme activity assays, offering insights into how HflKC and FtsH assemble into cage-shaped holoenzymes and how HflKC modulates FtsH activity.

RESULTS

The overall structure of the entire FtsH-HflKC complex

The FtsH-HflKC complex was purified in *E. coli* and showed ATPase and protease activity in *in vitro* ATPase and protease assays (Figures S1A–S1D); we next made efforts to determine its structure. During the initial cryo-EM data processing, we were not able to obtain a decent map for the cytosolic domain of FtsH, likely due to its extreme flexibility. Subsequently, we introduced two mutations (E252Q in the Walker B motif and E415Q in the HExxH motif) to stabilize the FtsH cytosolic domain, following an approach similar to a previously published one (Puchades et al., 2017, 2019). These mutations eventually led to the determination of the entire FtsH-HflKC complex structure (Figures S1E, S1F, and S2; Table S1). The overall architecture resembles a "bell-shaped" cage, and the HflKC complex forms the cage enclosing four FtsH homohexamers, with the periplasmic domain ($FtsH^{PD}$) and transmembrane regions ($FtsH^{TM}$) buried inside the cage and the cytoplasmic domains ($FtsH^{CD}$) situated at the base (Figure 1A; Video S1). During the data processing, we also observed some classes containing less than four FtsH homohexamers, which we deemed partial complex states. HflK and HflC are packed side by side with 12 copies of each protein forming the cage. Interestingly, the "bell crown," with a diameter of 115 Å, is formed from the C-terminal regions of both HflK and HflC (Figures 1A and 1B). In the center of the cage cap, there is a "pore" with a diameter of ~18 Å formed only by the 12 HflK subunits. The "bell waist" was formed by a total of 24 long α helices that are composed of the 12 HflK and 12 HflC subunits and are periodically arranged one by one (Figures 1A and 1B). In the case of FtsH, even though four hexameric $FtsH^{PD+TM}$ can be clearly seen interacting with the HflKC complex, only two $FtsH^{CD}$ showed concrete densities. Interestingly, the $FtsH^{CD}$ was observed to be tilted by ~15° at the axis relative to that of the HflKC cage (Figure 1A). As the FtsH-HflKC complex is too large and dynamic, especially for the $FtsH^{CD}$, we proceeded with subregion subtraction in Relion 3.1 to improve the subregion resolution (Scheres, 2012). Based on the consensus refinement map of the entire FtsH-HflKC complex, the $FtsH^{PD+TM}$-HflKC, the FtsH full-length hexamer, $FtsH^{PD+TM}$, and $FtsH^{CD}$ were subtracted and subjected to focused three-dimensional (3D) classification, autorefinement, and CTF refinement with final resolutions of approximately 4.0, 6.1, 6.5, and 3.3 Å with symmetry (C4, C1, C1, and C6) imposed, respectively (Figures S2 and S3).

HflK and HflC structure and assembly with FtsH

The structure of the HflKC complex, which forms the main body of the entire bell-shaped FtsH holoenzyme, together with $FtsH^{PD}$ and $FtsH^{TM}$ was reconstructed at an ~4.0 Å resolution (Figures 2A, S2, and S3; Table S1). For HflK, the structure is composed of a partially resolved transmembrane N-terminal helix α1, a β-fold (β1–β3) subdomain, and a PHB domain, followed by an arc-shaped long helix (α6), a short helix (α7), and two

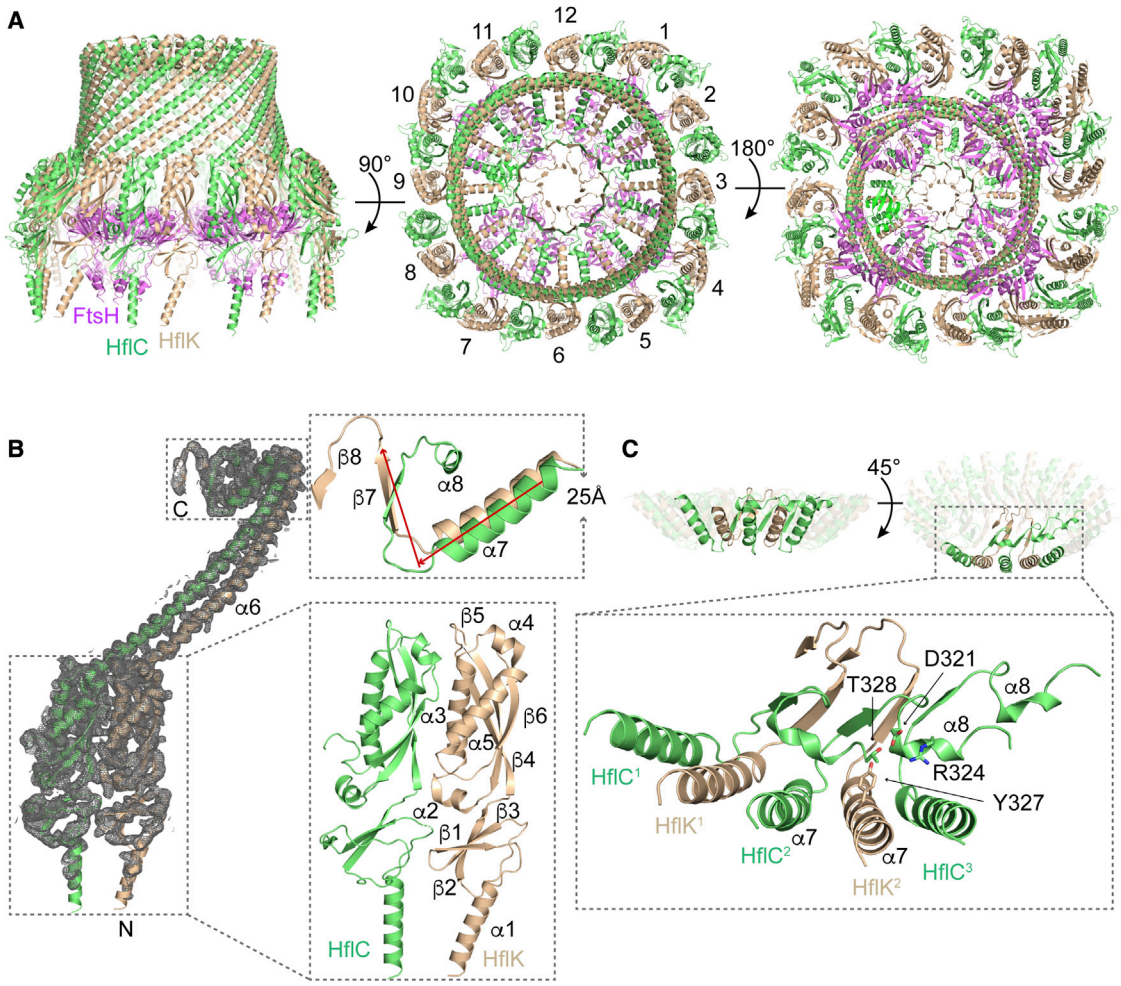

Figure 2. Structure of the FtsH^{PD+TM}-HflKC complex

(A) Structure of FtsH^{PD+TM}-HflKC. HflK, HflC, and FtsH are colored wheat, lime, and violet, respectively. The 12 HflKC heterodimers are numbered in the top view.

(B) The structure of the HflK and HflC subunits fitted to the cryo-EM map. The secondary-structure elements of HflK and HflC are labeled. Close-up views of the core domain and the C-terminal region for both proteins are presented on the right. The V-shaped turn between α7 and β7 is indicated by the red arrows. The β barrel at the cage center is formed exclusively by the C-terminal β8 from the 12 HflK subunits.

(C) Compact stacking of the cagecap involving the C termini of HflK and HflC. In particular, the HflC^1 C-terminal residues T328 not only interacts with D321 and R324 from the other consecutive subunits HflC^2 but also interacts with Y327 from HflK^2, forming a circular interaction linkage to stabilize the cap.

See also Figures S3–S7 and S9 and Tables S2 and S3.

strands (β7–β8) at the C terminus (Figure 2B). The evolutionarily conserved PHB domain consists of a curved antiparallel β sheet (β4–β6), with two helices (α3 and α5) occupying the β-sheet groove. In addition, α2 and α4 are parallel to each other, aligned perpendicularly to the sheet and located on its either side (Figure 2B). α6, α7, β7, and β8 from the C-terminal region of HflK form a zigzag arrangement that consequently serves as the building block for both the crown and the waist of the entire bellcomplex. Notably, all of the C-terminal β8 strands from the 12 HflK form a β barrel, with a central pore ~18 Å in diameter (Figures 1B and 2A). Although the protein sequences of HflK and HflC are not conserved, with only ~30% residue identity (Figure S4), the overall structure of HflC is very similar to that of HflK, with a root-mean-square deviation (RMSD) of 3.61 Å for all main-chain atoms, except that HflC has a short α8 helix following the β7 strand at its C terminus (Figure S5A).

The 12 HflK and HflC proteins interact extensively and reciprocally to form the entire HflKC complex. Given that the FtsH-HflKC complex shows C4 symmetry, we take the asymmetric unit (one-quarter of the entire structure), in which three pairs of HflKC dimers are tandemly arranged to interact with the FtsH hexamer, as a representative building block for illustration (Figure S5B). These three pairs of HflKC dimers aligned well overall, but the relative positioning of PHB domains, the long α6 helix, and the "cap" region of HflK and HflC varies to some extent (Figures S5C and S5D). To simplify these extensive contacts between HflK and HflC, we take one pair of HflK and HflC that contributes the most to the coordination of FtsH (Figures 2B, S5, and S6). The PHB domains of HflK and HflC compact each other,

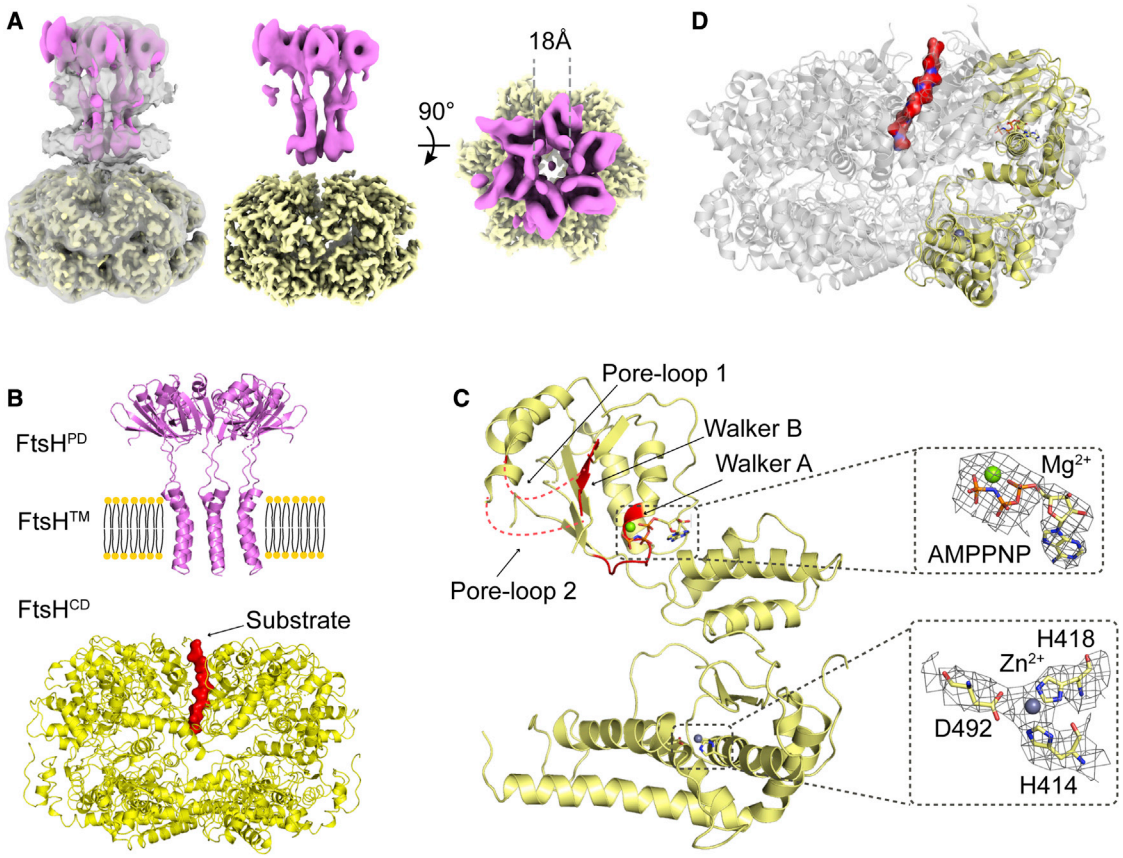

Figure 3. Structures of the full-length FtsH, FtsH^{PD+TM}, and FtsH^{CD}

(A) The isolated FtsH^{CD} map (yellow) and FtsH^{PD+TM} map (violet) are fitted into the full-length FtsH hexamer map (gray). The tunnel (with a diameter of ~18 Å) inside the hexameric FtsH is shown. This tunnel is formed by the periplasmic domain and the 2nd transmembrane helix of the hexameric FtsH.

(B) Structure of the FtsH hexamer. The bound peptide from human AFG3L2 is also shown based on the structural alignment shown in (A) and (D). The transmembrane region is indicated with two curved dashed lines.

(C) Structure of one FtsH^{CD} monomer with the functionally important motifs labeled. The bound AMPPNP is shown in sticks, and Mg^{2+} and Zn^{2+} ions are shown as spheres (colored green and blue, respectively). The gray mesh indicates the cryo-EM map.

(D) Structural comparison of FtsH^{CD} (yellow) and the human AFG3L2 cytosolic domain (PDB: 6NYY, gray). The substrate peptide of human AFG3L2 is shown on the surface and colored red.

See also Figures S3, S6, and S10.

involving a number of direct contacts (Figure S7A). The long α6 helix of HflK is flanked by two other parallel α6 helices of the two neighboring HflC subunits (Figure S7B). These interactions consist mainly of electrostatic interactions and Pi effects involving a number of arginine and aromatic residues (Tyr and Phe) (Tables S2 and S3). In addition, hydrophobic interactions also contribute to the helical packing. Notably, there are some sites where a network of interactions involving HflK and both HflC subunits are observed (such as R291 in the middle HflK interacting with M271 and Y255 in the left and right HflC, respectively), thereby greatly enhancing the stability of the complex (Figure S7B). Following the C terminus of this long helix α6, the sequential helix α7 and strand β7 in both HflK and HflC form a zigzag "V-shaped" arrangement (~25 Å in height), together with the HflC α8 helix and HflK β8 strand, and intertwine together to establish further contacts (Figures 2B and S7C). Due to the different orientation from the HflC α8 helix, only these ending β8 stands in HflK form parallel β sheets with each other, thereby constructing a pore at the center of the cap (Figures 2A and 2B). The distal HflC T328 not only interacts with D321 and R324 from the other HflC subunit, which is separated by one HflK chain, but also directly interacts with Y327 on HflK α7, which is separated by one HflC and one HflK (Figures 2C and S6). Therefore, the end-to-end association of the 12 HflC C termini builds a circular link, together with a network of interactions involving all of the α7-β7 of HflK and HflC, establishing a stable cap (Figures 2A and 2C).

Structure of the hexameric full-length FtsH

It has been very challenging to achieve a high-resolution full-length FtsH structure. Here, we managed to determine the structure of a hexameric full-length FtsH embedded in detergent micelles at a 6.1 Å resolution without applying symmetry (Figures 3A, S2, and S3; Table S1). The present structure is

composed of the N-terminal FtsH^{PD} arranged as a hexamer at the "top," followed by FtsH^{TM} in the "middle," and the hexameric FtsH^{CD} (including both the ATPase and the protease domains) at the "bottom." Interestingly, the entire reconstruction of the hexameric FtsH is similar to that of *A. aeolicus* FtsH in a nontilted form at low resolution (Carvalho et al., 2021). To better resolve the full-length FtsH map, the top part, including the FtsH^{PD+TM}, and the lower part, FtsH^{CD}, were separately subtracted and refined. This approach consequently yielded a clear map showing the transmembrane helices in FtsH^{PD+TM} as well as a distinguishable map for the ligand AMPPNP-bound FtsH^{CD} (Figures 3A–3C, S2, and S3). FtsH consists of two transmembrane helices located at its N terminus on either side of the hexameric FtsH^{PD} (Figure S1A). For the first time, the 2nd transmembrane helix and its linker to the FtsH^{PD} could be modeled (Figures 3A, 3B, and S6). Interestingly, a total of 6 helices from the FtsH hexamer pack to form a transmembrane cylinder with an inner pore diameter of ~18 Å. Following the 2nd transmembrane helix, each FtsH inside the homohexamer FtsH^{PD} contained an AMPPNP and a Mg^{2+} ion in the ATPase domain as well as a Zn^{2+} ion in the protease domain (Figure 3C). Comparison of the present structure with that of the human peptide-bound AFG3L2 reveals that our AMPPNP-bound FtsH resembles AFG3L2 in an ATP-bound state, with an RMSD of 1.87 Å over the main-chain atoms (Figure 3D). Notably, the bound peptide based on the above structural comparison was found to be oriented toward the transmembrane cylinder channel (Figure 3B).

FtsH interaction with HflKC and the entire FtsH holoenzyme assembly

The interactions between the hexameric FtsH^{PD} and the HflKC complex can be identified based on our structure (Figures 4A, S7D, and S7E). In a hexameric FtsH^{PD}, two adjacent subunits make contacts with two HflK proteins that are separated by one HflC. In one FtsH subunit, the β2-β3-turn loop (residues K61, D62, and S63) forms tight contacts with β4 in HflK. In particular, the hydroxyl group of FtsH S63 forms a hydrogen bond with the guanidinium group of HflK R141. The O atom of the FtsH K61 main chain interacts with the N atom of the HflK E142 main chain, and the amino group (side chain) of FtsH K61 is in close vicinity of the carboxylic group (side chain) of HflK E142. In addition, FtsH Q45 interacts with the HflK R185 via their side chains. Similarly, the β2-β3-turn loop in the neighboring FtsH subunit interacts with the next (separated by one HflC monomer) HflK β4. However, the two aforementioned residues, FtsH Q45 and HflK R185, are too far apart to form any interaction in the case of this FtsH monomer. The remaining three FtsH^{PD} hexamers interact with two HflK monomers separated by HflC in a similar manner. Additionally, each of the four FtsH^{PD} hexamers is packed to the next one through the β2-β3-turn loop in one hexamer, which wedges into a cleft formed between the two subunits of the next hexamer (α1 and its prior loop in one subunit, β4 in another) (Figure 4B). The packing mainly involves polar side chains and helps to stabilize the entire complex. Surprisingly, the 2nd transmembrane helix of FtsH resolved in our structure appears not to contact either HflK/HflC or other FtsH hexamers. FtsH^{CD} does not interact with one another, which could increase the structural flexibility required for its activity. Interestingly, despite the overall similarity of the present hexameric FtsH^{PD} and the crystal structure of FtsH periplasmic domain (Scharfenberg et al., 2015), we do observe a shift of the β2-β3-loop region in FtsH^{PD} by 1–2 Å toward HflK upon formation of their interacting complex through structural comparison (Figure S5E).

Structure-based mutagenesis and activity assay

To analyze how important these interactions observed in our structure (Figure 4A) are for the formation of the entire complex as well as to study their effect on *in vivo* enzymatic activity, we generated FtsH mutants (D62F, Q45A, and K61A/D62A/S63A triple mutation) along the interface between FtsH and HflK. First, we investigated the interaction between the FtsH mutants with a C-terminal His_6-Myc bipartite tag (FtsH-His_6-Myc) and HflKC by a pull-down assay using Ni-NTA agarose (Figure 5A). As shown in Figures 5A, 5C, and 5D, we found that HflK was artificially cleaved to generate a degradation product (HflK') upon membrane solubilization, and as a result, the cellular level of full-length HflK was significantly lower in the strains expressing the FtsH K61A/D62A/S63A and D62F mutants compared with strains expressing wild-type or the Q45A mutant of FtsH, but the level of HflC was not apparently altered in these strains (Tables S4 and S5). Therefore, we calculated the ratio of the imidazole-eluted HflC, HflK' and full-length HflK to the total HflC, total HflK' and total HflK, respectively, in the flow through, wash, and eluate fractions combined (Figures 5B and S8A). The results showed that the recovery of HflC and HflK in the eluate was significantly decreased by the K61A/D62A/S63A and D62F mutations but not by the Q45A mutation, strongly suggesting that the K61A/D62A/S63A and D62F mutations impaired the interaction between FtsH and HflKC (Figures 5B and S8A).

Finally, we examined how the aforementioned FtsH residues implicated in the formation and/or stabilization of the entire complex would affect the protease activity of FtsH *in vivo*. To this end, we analyzed the degradation of two proteins, CII and SecY, in strains (Tables S4 and S5) expressing FtsH mutants (K61A/D62A/S63A, D62F, and Q45A). For the CII *in vivo* degradation assay, both CII and FtsH expression were induced in AK525 cells (the cellular amount of FtsH was decreased in this strain), and the stability of CII was examined by pulse-chase experiments. We found that CII degradation was significantly slower in the strains expressing the FtsH (K61A/D62A/S63A) and FtsH (D62F) mutants than in the strain expressing the wild-type FtsH (Figures 5E and S8B). These findings strongly suggest that these mutations dramatically affected the FtsH-HflKC interaction given that similar observations have been made with the deletion of the periplasmic region of FtsH, which resulted in abolishing complex formation of FtsH with HflKC (Akiyama et al., 1998). The Q45A mutation exerted no detectable effect on the degradation of CII by FtsH (Figures 5E and S8B). This is consistent with the pull-down assay results as well as our structural data suggesting that the Q45 residue may only weakly affect the FtsH-HflKC interaction. We also examined the FtsH-dependent degradation of the C-terminally His_6-Myc-tagged SecY (SecY-His_6-Myc). Expression of SecY-His_6-Myc and the mutant variants of FtsH-His_6-Myc were induced in AD1691 (Δ*ftsH* strain), and the accumulation levels of SecY were examined by immunoblotting

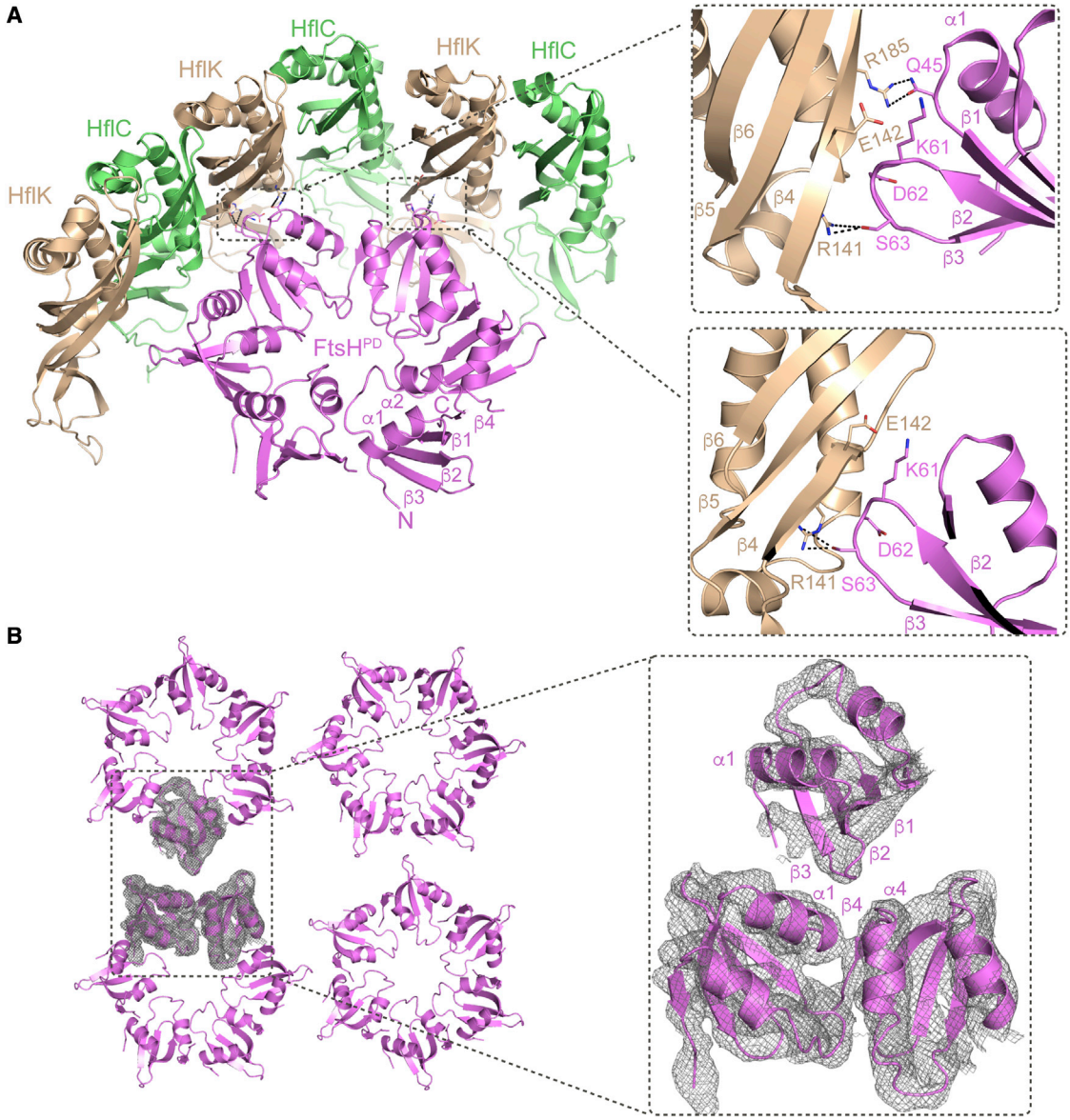

Figure 4. The assembly of the FtsH-HflKC complex

(A) The FtsH^{PD} hexamer interacts with the HflKC cage complex. The residues involved in the interaction are labeled and shown in sticks. The secondary-structure elements of FtsH^{PD} are labeled. The detailed interaction is shown on the right, with the residues labeled.

(B) Interior packing of the four FtsH^{PD} hexamers. The interaction interface is shown, and the involved secondary-structure elements are labeled. The gray mesh indicates the cryo-EM map.

See also Figures S3, S5–S7, S9, and S11.

(Figures 5F and S8C). As expected, the results showed that all the FtsH mutants were almost as active as the wild-type FtsH, which is in line with our previous results that the defective interaction between FtsH and HflKC has little influence on the degradation of SecY (Akiyama et al., 1998). Taken together, our results indicate that all FtsH mutants retain near-normal SecY degradation activity, whereas FtsH mutants K61A/D62A/S63A and D62F showed significantly defective CII degradation activities *in vivo*. The results of the pull-down and *in vivo* degradation assays are consistent with our structural data, suggesting that K61A/D62A/S63A and D62F mutations would impair the FtsH-HflKC interaction.

DISCUSSION

The essential role of FtsH in protein degradation involves either quality control of misfolded/malfunction proteins or conditional (i.e., under certain stress) proteolysis of unimpaired proteins (Begg et al., 1992; Kihara et al., 1995; Santos and De Almeida, 1975; Tomoyasu et al., 1993a, 1993b). The HflKC complex

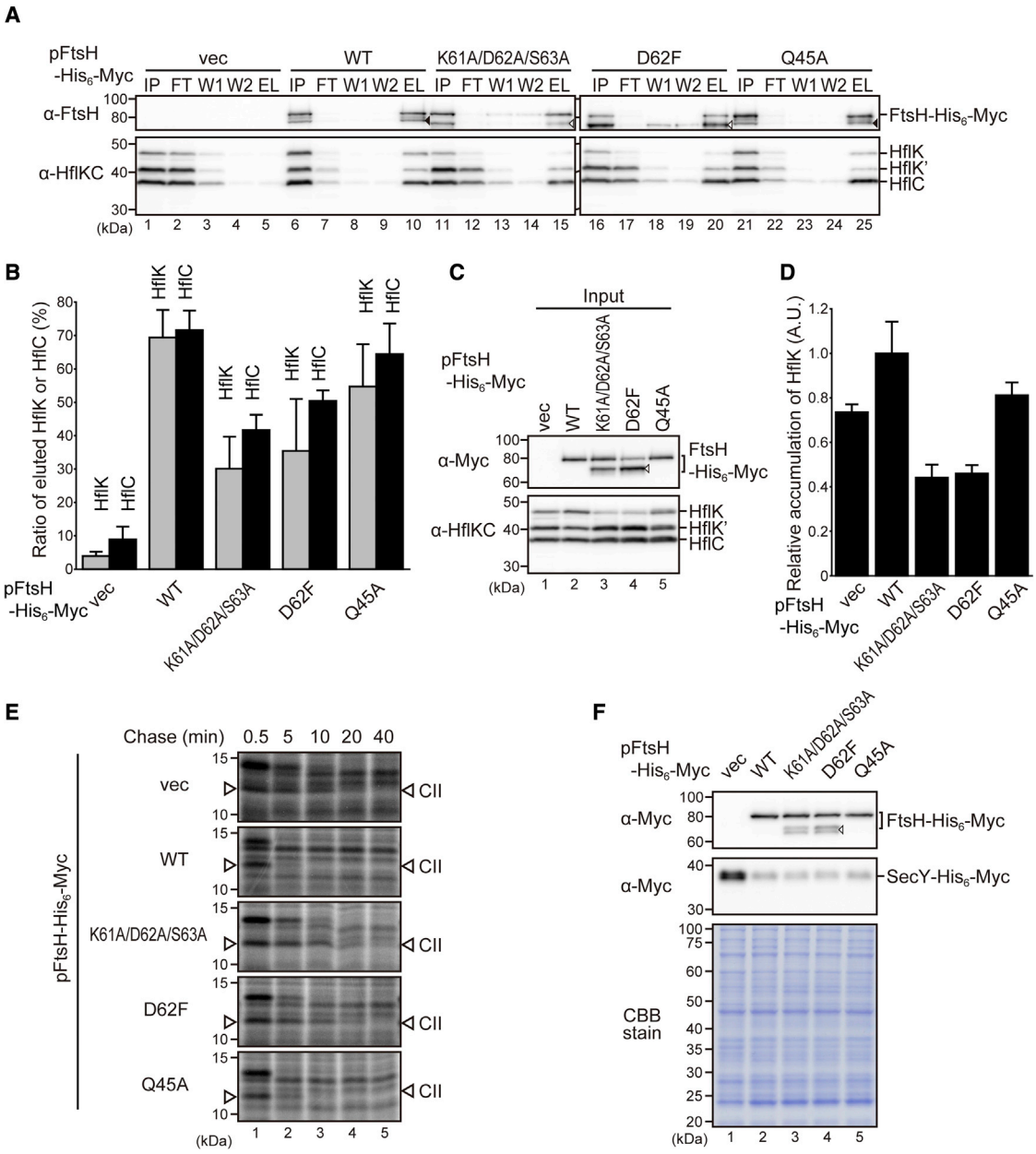

Figure 5. Pull-down and *in vivo* degradation assays of FtsH

(A) Pull-down assay of FtsH tagged with His_6-Myc (FtsH-His_6-Myc) wild-type (WT) and mutant (K61A/D62A/S63A, D62F, and Q45A) FtsH were used. Proteins in input (IP), flow-through (FT), first-wash (W1), second-wash (W2), and eluate (EL) fractions were analyzed by 10% Laemmli SDS-PAGE. Anti-FtsH (α-FtsH) and anti-HflKC (α-HflKC) antibodies were used for immunoblotting. The open and closed arrowheads in (A), (C), and (F) indicate the C- and N terminally cleaved products of FtsH-His_6-Myc, respectively. HflK' indicates a degradation product of HflK.

(B) Quantification of the FtsH pull-down assay shown in (A). The band intensities of HflC and HflK in all fractions were quantified, and the percentage of the band intensity in the EL fraction compared with the total band intensity (in FT, W1, W2, and EL fractions) was calculated. The average values of three independent experiments with standard deviations are shown.

(C) Accumulation of HflKC in the presence of FtsH-His_6-Myc mutants. The proteins in the IP fraction shown in (A) were reanalyzed by SDS-PAGE and used instead anti-Myc (α-Myc) for immunoblotting.

(D) Quantification of the results shown in (C). The band intensities of HflK were quantified, and the average values from three independent experiments with standard deviations are shown.

(E) FtsH protease activity assay. Degradation of CII by WT and mutant FtsH was analyzed. The cells were pulse labeled with [^{35}S] methionine for 30 s followed by chasing with an excess amount of unlabeled methionine for 0.5, 5, 10, 20, and 40 min.

(F) FtsH protease activity assay. The degradation of SecY by WT and mutant FtsH was analyzed. Proteins were analyzed by 10% SDS-PAGE and α-Myc immunoblotting to visualize FtsH-His_6-Myc and its mutants as well as SecY-His_6-Myc.

See also Figure S8 and Tables S4 and S5.

interacts with FtsH to finely modulate its proteolytic activity. However, the entire architecture remains a long-standing mystery. Here, we determined the structure of a nearly intact FtsH-HflKC complex, which exhibits a bell-shaped cage (Figure 1A). Our structure identified that the β2-β3-turn loop from two adjacent subunits of $FtsH^{PD}$ dominantly interacts with 2 HflK subunits separated by one HflC molecule (Figure 4A). Our functional data further demonstrate that the β2-β3-turn loops (residues K61, D62, and S63) of the periplasmic domain of FtsH are essential for the assembly of the entire FtsH-HflKC complex based on mutagenesis with pull-down assays and *in vivo* proteolytic activity assays (Figure 5). These findings are in line with those of a previous report that the truncation of the periplasmic domain of FtsH greatly decreased its proteolytic activity against CII but had little effect on its activity against SecY (Akiyama et al., 1998). Comparison of our structure with a recently published one showed that, overall, they are consistent for HflKC assembly and the interaction interface between the $FtsH^{PD}$ hexamer and the cage complex HflKC (Figure S9). Note that our structure is additionally presented with cytoplasmic domains of FtsH (both ATP-binding and proteolytic domains, including ligands such as AMPPNP and metal ions Mg^{2+} and Zn^{2+} at the active site), which was determined at ~3.3 Å resolution (Figure 3). Moreover, the 2^{nd} transmembrane helix region of FtsH, with 6 helices of FtsH hexamer forming a cylinder-shaped barrel, was illustrated in our structure (Figures 3 and S9). To facilitate a better understanding of our structure, we generated a short movie to demonstrate the assembly of the FtsH-HflKC complex and its structural features (Video S1).

Recently, a total of 21 proteins in *E. coli* were identified as FtsH substrates, including diverse membrane proteins and cytosolic proteins (Bittner et al., 2017). How is the substrate specificity (particularly for membrane proteins and cytosolic proteins), as well as conditional protease activity, regulated? We have reported previously that in Δ*hflKC* cells or cells expressing an FtsH mutant defective in the interaction with HflKC, the degradation of soluble substrates such as CII is retarded (Akiyama et al., 1998). In contrast, degradation of SecY24 (a SecY mutant defective in interaction with SecE, another component of the translocon) is significantly accelerated in the absence of HflKC (Kihara et al., 1996). Additionally, the *hflK13* and *hflC9* mutations as well as YccA11, a mutant form of membrane substrate YccA, interferes with the degradation of membrane substrates but little affects that of soluble substrates. Thus, we proposed a model in which FtsH-associated HflKC acts as a regulator to negatively modulate FtsH activity to degrade membrane substrates (Ito and Akiyama, 2005). It has been suggested that the absence of HflKC might affect the degradation of cytoplasmic substrates, as under this condition, FtsH is exposed more to membrane substrates. Our structure matches this proposal, as the membrane and periplasmic regions of FtsH are shielded by HflKC molecules to prevent FtsH from degrading normal functional membrane proteins.

HflKC also seems to act in a stable association with membrane substrates once it is directed to FtsH, as we have previously shown that YccA11 can be cross-linked with FtsH/HflKC in a HflKC-dependent manner *in vivo* (Kihara et al., 1998). An *in vitro* study with purified proteins demonstrated that HflKC has a YccA-binding ability in the absence of FtsH (Kihara et al., 1998). It is thus possible that HflKC can function as an adaptor to bind and present substrates to FtsH. Apart from the HflK Q347-E419 region, two more regions are disordered and not modeled in our structure, which are HflC G158-I193 and HflK M1-Q75. These two disordered regions could be involved in membrane and cytosolic protein specificity recognition and recruitment directly or indirectly to FtsH. Moreover, there is a central pore (~18 Å in diameter) at the cage cap formed by HflKC (specifically HflK) (Figure 1B). The resolution of the pore region is not high enough to clearly model all the side chains, which does not allow us to interpret this pore's surface property unambiguously. Nevertheless, it appears to be amphipathic. Interestingly, a pathway ~18 Å in diameter is also formed by the enclosed $FtsH^{PD}$ hexamer followed by the $FtsH^{TM}$ (Figures 1B and 3A). Superposition of the substrate-bound human m-AAA protease AFG3L2 (Puchades et al., 2019) to the present complex reveals that the substrate is perfectly oriented toward this pore (Figure 3). Note that the dimensions of the pore observed in our structure are in a similar range to the nascent polypeptide exit channel in the ribosome (Feng et al., 2013; Su et al., 2018), which enables unfolded polypeptide to go through, although it is unclear if the specificity of such polypeptide is required or not for FtsH. Therefore, HflKC likely modulates an alternative pathway for the substrates and/or matrix substance to access from the periplasmic side, in addition to access from the cytoplasmic side (Figure S10). The pore of the cap HflKC appears to be quite far to that of the $FtsH^{CD}$, with a distance of ~200 Å, and there is no report on a periplasmic protein substrate of FtsH-HflKC, so further study is required to investigate this proposed pathway. Nevertheless, the present structure of the entire FtsH holoenzyme raises an interesting possibility of its novel cellular role in periplasmic protein quality control. Overall, the HflKC complex has a microcompartment effect on FtsH, eventually regulating FtsH activity. Indeed, it was reported that HflKC has no influence on both the activity and specificity of FtsH *in vitro*, which perhaps correlates with this microcompartment effect (Akiyama et al., 1998).

SPFH-domain-containing proteins are universally conserved from bacteria to humans. HflK and HflC are members of this protein family, and other SPFH proteins could also form such cage-like structures (Daumke and Lewin, 2022). For example, an even larger cage structure has been reported for a rat liver vault, although its cellular function is unclear (Tanaka et al., 2009). These SPFH proteins forming a cage would be of great interest for future studies to determine the precise function of this intriguing structure, particularly the prohibitin complex that interacts with the human m-AAA protease AFG3L2 to regulate its activity. Considering the similar domain organization between *E. coli* FtsH-HflKC and the human AFG3L2-prohibitin complex, it is plausible that the human AFG3L2-prohibitin complex assembles similarly to our FtsH-HflKC complex. Indeed, the nuclear magnetic resonance (NMR) structure of the human m-AAA protease AFG3L2 periplasmic domain aligns well with $FtsH^{PD}$ (Ramelot et al., 2013). Furthermore, the model predicted by Alphafold2 of the PHB domain of human prohibitin 1 also aligns well with HflK, enabling us to generate a model to demonstrate

how AFG3L2 and prohibitin likely assemble into a functional complex (Jumper et al., 2021) (Figure S11). Given that the prohibitin complex has been implicated in various functions and that its dysfunction is directly linked to diseases (Back et al., 2002; Nijtmans et al., 2002), our findings offer structural information to better understand the pathogenesis of these aging-associated diseases.

Limitations of the study

The overall resolution of FtsH-HflKC is a bit low (~6.8 Å), possibly because the $FtsH^{CD}$ is flexibly tethered to the membrane. Moreover, the FtsH-HflKC complex was chemically cross-linked to achieve a more stable state; the reported AMPPNP-bound $FtsH^{CD}$ structure with C6 symmetry imposed could differ from its physiologically catalytic state. Therefore, how FtsH recognizes and degrades its protein substrates is still unclear.

STAR★METHODS

Detailed methods are provided in the online version of this paper and include the following:

- KEY RESOURCES TABLE
- RESOURCE AVAILABILITY
  - Lead contact
  - Materials availability
  - Data and code availability
- EXPERIMENTAL MODEL AND SUBJECT DETAILS
- METHOD DETAILS
  - Cloning and site-directed mutagenesis
  - Media
  - Immunoblotting
  - Pulse-chase experiment
  - Pull-down assay
  - Protein expression and purification
  - Crosslinking of the FtsH-HflKC complex
  - *In vitro* ATPase and protease assays of the FtsH-HflKC complex
  - Negative staining electron microscopy
  - Cryo-EM

SUPPLEMENTAL INFORMATION

Supplemental information can be found online at https://doi.org/10.1016/j.celrep.2022.110890.

ACKNOWLEDGMENTS

This work was supported by a Tier II grant MOE2019-T2-2-099 and a Tier 1 grant RG108/20 from the Ministry of Education (MOE) of Singapore (Y.-G.G.). We thank Rya Ero and Eleanor Martin for their manuscript advice and Hiroyuki Mori for the plasmid pHM1530 construction.

AUTHOR CONTRIBUTIONS

Conceptualization, Y.-G.G., Y.A., and Z.Q.; methodology, Y.-G.G., Y.A., Z.Q., and T.Y.; formal analysis, Y.-G.G., Y.A., Z.Q., T.Y., X.-F.Y., and S.B; investigation, Z.Q., T.Y., and I.T.B.; resources, Y.-G.G., Y.A., and J.S.; writing – original draft, Y.-G.G., Y.A., Z.Q., and T.Y.; writing – review & editing: Y.-G.G., Y.A., Z.Q., and T.Y.; funding acquisition: Y.-G.G.; supervision: Y.-G.G. and Y.A.

DECLARATION OF INTERESTS

The authors declare that they have no conflicts of interest.

Received: March 31, 2022
Revised: April 25, 2022
Accepted: May 6, 2022
Published: May 31, 2022

REFERENCES

Adams, P.D., Afonine, P.V., Bunkoczi, G., Chen, V.B., Davis, I.W., Echols, N., Headd, J.J., Hung, L.W., Kapral, G.J., Grosse-Kunstleve, R.W., et al. (2010). PHENIX: a comprehensive Python-based system for macromolecular structure solution. Acta Crystallogr. D Biol. Crystallogr. *66*, 213–221. https://doi.org/10.1107/S0907444909052925.

Akiyama, Y., and Ito, K. (1985). The SecY membrane component of the bacterial protein export machinery: analysis by new electrophoretic methods for integral membrane proteins. EMBO J. *4*, 3351–3356. https://doi.org/10.1002/j.1460-2075.1985.tb04088.x.

Akiyama, Y., Kihara, A., Tokuda, H., and Ito, K. (1996). FtsH (HflB) Is an ATP-dependent Protease Selectively Acting on SecY and Some Other Membrane Proteins. J. Biol. Chem. *271*, 31196–31201. https://doi.org/10.1074/jbc.271.49.31196.

Akiyama, Y., Ogura, T., and Ito, K. (1994). Involvement of FtsH in protein assembly into and through the membrane. I. Mutations that reduce retention efficiency of a cytoplasmic reporter. J. Biol. Chem. *269*, 5218–5224. https://doi.org/10.1016/s0021-9258(17)37677-9.

Akiyama, Y., Kihara, A., Mori, H., Ogura, T., and Ito, K. (1998). Roles of the periplasmic domain of *Escherichia coli* FtsH (HflB) in protein interactions and activity modulation. J. Biol. Chem. *273*, 22326–22333. https://doi.org/10.1074/jbc.273.35.22326.

Back, J.W., Sanz, M.A., De Jong, L., De Koning, L.J., Nijtmans, L.G., De Koster, C.G., Grivell, L.A., Van Der Spek, H., and Muijsers, A.O. (2002). A structure for the yeast prohibitin complex: structure prediction and evidence from chemical crosslinking and mass spectrometry. Protein Sci. *11*, 2471–2478. https://doi.org/10.1110/ps.0212602.

Begg, K.J., Tomoyasu, T., Donachie, W.D., Khattar, M., Niki, H., Yamanaka, K., Hiraga, S., and Ogura, T. (1992). *Escherichia coli* mutant Y16 is a double mutant carrying thermosensitive ftsH and ftsI mutations. J. Bacteriol. *174*, 2416–2417. https://doi.org/10.1128/jb.174.7.2416-2417.1992.

Bieniossek, C., Schalch, T., Bumann, M., Meister, M., Meier, R., and Baumann, U. (2006). The molecular architecture of the metalloprotease FtsH. Proc. Natl. Acad. Sci. U S A *103*, 3066–3071. https://doi.org/10.1073/pnas.0600031103.

Bieniossek, C., Niederhauser, B., and Baumann, U.M. (2009). The crystal structure of apo-FtsH reveals domain movements necessary for substrate unfolding and translocation. Proc. Natl. Acad. Sci. U S A *106*, 21579–21584. https://doi.org/10.1073/pnas.0910708106.

Bittner, L.M., Arends, J., and Narberhaus, F. (2017). When, how and why? Regulated proteolysis by the essential FtsH protease in *Escherichia coli*. Biol. Chem. *398*, 625–635. https://doi.org/10.1515/hsz-2016-0302.

Brand, J., Smith, E.S.J., Schwefel, D., Lapatsina, L., Poole, K., Omerbasic, D., Kozlenkov, A., Behlke, J., Lewin, G.R., and Daumke, O. (2012). A stomatin dimer modulates the activity of acid-sensing ion channels. EMBO J. *31*, 3635–3646. https://doi.org/10.1038/emboj.2012.203.

Carvalho, V., Prabudiansyah, I., Kovacik, L., Chami, M., Kieffer, R., van der Valk, R., de Lange, N., Engel, A., and Aubin-Tam, M.E. (2021). The cytoplasmic domain of the AAA+ protease FtsH is tilted with respect to the membrane to facilitate substrate entry. J. Biol. Chem. *296*, 100029. https://doi.org/10.1074/jbc.RA120.014739.

Chen, B., Retzlaff, M., Roos, T., and Frydman, J. (2011). Cellular strategies of protein quality control. Cold Spring Harb. Perspect. Biol. *3*, a004374. https://doi.org/10.1101/cshperspect.a004374.

Chiba, S., Ito, K., and Akiyama, Y. (2006). The *Escherichia coli* plasma membrane contains two PHB (prohibitin homology) domain protein complexes of opposite orientations. Mol. Microbiol. *60*, 448–457. https://doi.org/10.1111/j.1365-2958.2006.05104.x.

Dalbey, R.E., Wang, P., and van Dijl, J.M. (2012). Membrane proteases in the bacterial protein secretion and quality control pathway. Microbiol. Mol. Biol. Rev. *76*, 311–330. https://doi.org/10.1128/MMBR.05019-11.

Daumke, O., and Lewin, G.R. (2022). SPFH protein cage - one ring to rule them all. Cell Res. *32*, 117–118. https://doi.org/10.1038/s41422-021-00605-7.

DeLano, W.L. (2002). PyMOL: an open-source molecular graphics tool. Ccp4 Newsl. Pro. Crystallogr.

Emsley, P., Lohkamp, B., Scott, W.G., and Cowtan, K. (2010). Features and development of coot. Acta Crystallogr. D Biol. Crystallogr. *66*, 486–501. https://doi.org/10.1107/S0907444910007493.

Feng, S., Chen, Y., and Gao, Y.G. (2013). Crystal structure of 70S ribosome with both cognate tRNAs in the E and P sites representing an authentic elongation complex. PLoS One *8*, e58829. https://doi.org/10.1371/journal.pone.0058829.

Ito, K., and Akiyama, Y. (2005). Cellular functions, mechanism of action, and regulation of FtsH protease. Annu. Rev. Microbiol. *59*, 211–231. https://doi.org/10.1146/annurev.micro.59.030804.121316.

Jumper, J., Evans, R., Pritzel, A., Green, T., Figurnov, M., Ronneberger, O., Tunyasuvunakool, K., Bates, R., Zidek, A., Potapenko, A., et al. (2021). Highly accurate protein structure prediction with AlphaFold. Nature *596*, 583–589. https://doi.org/10.1038/s41586-021-03819-2.

Kastner, B., Fischer, N., Golas, M.M., Sander, B., Dube, P., Boehringer, D., Hartmuth, K., Deckert, J., Hauer, F., Wolf, E., et al. (2008). GraFix: sample preparation for single-particle electron cryomicroscopy. Nat. Methods *5*, 53–55. https://doi.org/10.1038/nmeth1139.

Kihara, A., Akiyama, Y., and Ito, K. (1995). FtsH is required for proteolytic elimination of uncomplexed forms of SecY, an essential protein translocase subunit. Proc. Natl. Acad. Sci. U S A *92*, 4532–4536. https://doi.org/10.1073/pnas.92.10.4532.

Kihara, A., Akiyama, Y., and Ito, K. (1996). A protease complex in the *Escherichia coli* plasma membrane: HflKC (HflA) forms a complex with FtsH (HflB), regulating its proteolytic activity against SecY. EMBO J. *15*, 6122–6131. https://doi.org/10.1002/j.1460-2075.1996.tb01000.x.

Kihara, A., Akiyama, Y., and Ito, K. (1998). Different pathways for protein degradation by the FtsH/HflKC membrane-embedded protease complex: an implication from the interference by a mutant form of a new substrate protein, YccA. J. Mol. Biol. *279*, 175–188. https://doi.org/10.1006/jmbi.1998.1781.

Krzywda, S., Brzozowski, A.M., Verma, C., Karata, K., Ogura, T., and Wilkinson, A.J. (2002). The crystal structure of the AAA domain of the ATP-dependent protease FtsH of *Escherichia coli* at 1.5 A resolution. Structure *10*, 1073–1083. https://doi.org/10.1016/s0969-2126(02)00806-7.

Ma, C., Wang, C., Luo, D., Yan, L., Yang, W., Li, N., and Gao, N. (2022). Structural insights into the membrane microdomain organization by SPFH family proteins. Cell Res. *32*, 176–189. https://doi.org/10.1038/s41422-021-00598-3.

Mastronarde, D.N. (2005). Automated electron microscope tomography using robust prediction of specimen movements. J. Struct. Biol. *152*, 36–51. https://doi.org/10.1016/j.jsb.2005.07.007.

Miller, J.H. (1972). Experiments in Molecular Genetics (Cold Spring Harbor Laboratory).

Mori, H., Akiyama, Y., and Ito, K. (2003). A SecE mutation that modulates SecY-SecE translocase assembly, identified as a specific suppressor of SecY defects. J. Bacteriol. *185*, 948–956. https://doi.org/10.1128/JB.185.3.948-956.2003.

Nijtmans, L.G., de Jong, L., Artal Sanz, M., Coates, P.J., Berden, J.A., Back, J.W., Muijsers, A.O., van der Spek, H., and Grivell, L.A. (2000). Prohibitins act as a membrane-bound chaperone for the stabilization of mitochondrial proteins. EMBO J. *19*, 2444–2451. https://doi.org/10.1093/emboj/19.11.2444.

Nijtmans, L.G., Artal Sanz, M., Artal, S.M., Grivell, L.A., and Coates, P.J. (2002). The mitochondrial PHB complex: roles in mitochondrial respiratory complex assembly, ageing and degenerative disease. Cell Mol. Life Sci. *59*, 143–155. https://doi.org/10.1007/s00018-002-8411-0.

Niwa, H., Tsuchiya, D., Makyio, H., Yoshida, M., and Morikawa, K. (2002). Hexameric ring structure of the ATPase domain of the membrane-integrated metalloprotease FtsH from *Thermus thermophilus HB8*. Structure *10*, 1415–1423. https://doi.org/10.1016/s0969-2126(02)00855-9.

Pettersen, E.F., Goddard, T.D., Huang, C.C., Couch, G.S., Greenblatt, D.M., Meng, E.C., and Ferrin, T.E. (2004). UCSF Chimera–a visualization system for exploratory research and analysis. J. Comput. Chem. *25*, 1605–1612. https://doi.org/10.1002/jcc.20084.

Pettersen, E.F., Goddard, T.D., Huang, C.C., Meng, E.C., Couch, G.S., Croll, T.I., Morris, J.H., and Ferrin, T.E. (2021). UCSF ChimeraX: structure visualization for researchers, educators, and developers. Protein Sci. *30*, 70–82. https://doi.org/10.1002/pro.3943.

Puchades, C., Rampello, A.J., Shin, M., Giuliano, C.J., Wiseman, R.L., Glynn, S.E., and Lander, G.C. (2017). Structure of the mitochondrial inner membrane AAA+ protease YME1 gives insight into substrate processing. Science *358*, eaao0464. https://doi.org/10.1126/science.aao0464.

Puchades, C., Ding, B., Song, A., Wiseman, R.L., Lander, G.C., and Glynn, S.E. (2019). Unique structural features of the mitochondrial AAA+ protease AFG3L2 reveal the molecular basis for activity in health and disease. Mol. Cell *75*, 1073–1085.e6. https://doi.org/10.1016/j.molcel.2019.06.016.

Ramelot, T.A., Yang, Y., Sahu, I.D., Lee, H.W., Xiao, R., Lorigan, G.A., Montelione, G.T., and Kennedy, M.A. (2013). NMR structure and MD simulations of the AAA protease intermembrane space domain indicates peripheral membrane localization within the hexaoligomer. FEBS Lett. *587*, 3522–3528. https://doi.org/10.1016/j.febslet.2013.09.009.

Rohou, A., and Grigorieff, N. (2015). CTFFIND4: fast and accurate defocus estimation from electron micrographs. J. Struct. Biol. *192*, 216–221. https://doi.org/10.1016/j.jsb.2015.08.008.

Saikawa, N., Akiyama, Y., and Ito, K. (2004). FtsH exists as an exceptionally large complex containing HflKC in the plasma membrane of *Escherichia coli*. J. Struct. Biol. *146*, 123–129. https://doi.org/10.1016/j.jsb.2003.09.020.

Sanchez-Garcia, R., Gomez-Blanco, J., Cuervo, A., Carazo, J.M., Sorzano, C.O.S., and Vargas, J. (2021). DeepEMhancer: a deep learning solution for cryo-EM volume post-processing. Commun. Biol. *4*, 874. https://doi.org/10.1038/s42003-021-02399-1.

Santos, D., and De Almeida, D.F. (1975). Isolation and characterization of a new temperature-sensitive cell division mutant of *Escherichia coli* K-12. J. Bacteriol. *124*, 1502–1507. https://doi.org/10.1128/jb.124.3.1502-1507.1975.

Scharfenberg, F., Serek-Heuberger, J., Coles, M., Hartmann, M.D., Habeck, M., Martin, J., Lupas, A.N., and Alva, V. (2015). Structure and evolution of N-domains in AAA metalloproteases. J. Mol. Biol. *427*, 910–923. https://doi.org/10.1016/j.jmb.2014.12.024.

Scheres, S.H. (2012). A Bayesian view on cryo-EM structure determination. J. Mol. Biol. *415*, 406–418. https://doi.org/10.1016/j.jmb.2011.11.010.

Shimohata, N., Chiba, S., Saikawa, N., Ito, K., and Akiyama, Y. (2002). The Cpx stress response system of *Escherichia coli* senses plasma membrane proteins and controls HtpX, a membrane protease with a cytosolic active site. Genes Cells *7*, 653–662. https://doi.org/10.1046/j.1365-2443.2002.00554.x.

Shimoike, T., Taura, T., Kihara, A., Yoshihisa, T., Akiyama, Y., Cannon, K., and Ito, K. (1995). Product of a new gene, syd, functionally interacts with SecY when overproduced in *Escherichia coli*. J. Biol. Chem. *270*, 5519–5526. https://doi.org/10.1074/jbc.270.10.5519.

Silhavy, T.J., Berman, M.L., and Enquist, L.W. (1984). Experiments with Gene Fusions (Cold Spring Harbor, New York: Cold Spring Harbor Laboratory Press).

Su, W., Kumar, V., Ding, Y., Ero, R., Serra, A., Lee, B.S.T., Wong, A.S.W., Shi, J., Sze, S.K., Yang, L., and Gao, Y.G. (2018). Ribosome protection by antibiotic

resistance ATP-binding cassette protein. Proc. Natl. Acad. Sci. U S A *115*, 5157–5162. https://doi.org/10.1073/pnas.1803313115.

Suno, R., Niwa, H., Tsuchiya, D., Zhang, X., Yoshida, M., and Morikawa, K. (2006). Structure of the whole cytosolic region of ATP-dependent protease FtsH. Mol. Cell *22*, 575–585. https://doi.org/10.1016/j.molcel.2006.04.020.

Suno, R., Shimoyama, M., Abe, A., Shimamura, T., Shimodate, N., Watanabe, Y.H., Akiyama, Y., and Yoshida, M. (2012). Conformational transition of the lid helix covering the protease active site is essential for the ATP-dependent protease activity of FtsH. FEBS Lett. *586*, 3117–3121. https://doi.org/10.1016/j.febslet.2012.07.069.

Tanaka, H., Kato, K., Yamashita, E., Sumizawa, T., Zhou, Y., Yao, M., Iwasaki, K., Yoshimura, M., and Tsukihara, T. (2009). The structure of rat liver vault at 3.5 angstrom resolution. Science *323*, 384–388. https://doi.org/10.1126/science.1164975.

Tatsuta, T., Model, K., and Langer, T. (2005). Formation of membrane-bound ring complexes by prohibitins in mitochondria. Mol. Biol. Cell *16*, 248–259. https://doi.org/10.1091/mbc.e04-09-0807.

Tomoyasu, T., Yamanaka, K., Murata, K., Suzaki, T., Bouloc, P., Kato, A., Niki, H., Hiraga, S., and Ogura, T. (1993a). Topology and subcellular localization of FtsH protein in *Escherichia coli*. J. Bacteriol. *175*, 1352–1357. https://doi.org/10.1128/jb.175.5.1352-1357.1993.

Tomoyasu, T., Yuki, T., Morimura, S., Mori, H., Yamanaka, K., Niki, H., Hiraga, S., and Ogura, T. (1993b). The *Escherichia coli* FtsH protein is a prokaryotic member of a protein family of putative ATPases involved in membrane functions, cell cycle control, and gene expression. J. Bacteriol. *175*, 1344–1351. https://doi.org/10.1128/jb.175.5.1344-1351.1993.

Tomoyasu, T., Gamer, J., Bukau, B., Kanemori, M., Mori, H., Rutman, A.J., Oppenheim, A.B., Yura, T., Yamanaka, K., Niki, H., et al. (1995). *Escherichia coli* FtsH is a membrane-bound, ATP-dependent protease which degrades the heat-shock transcription factor sigma 32. EMBO J. *14*, 2551–2560. https://doi.org/10.1002/j.1460-2075.1995.tb07253.x.

Vostrukhina, M., Popov, A., Brunstein, E., Lanz, M.A., Baumgartner, R., Bieniossek, C., Schacherl, M., and Baumann, U. (2015). The structure of *Aquifex aeolicus* FtsH in the ADP-bound state reveals a C2-symmetric hexamer. Acta Crystallogr. D Biol. Crystallogr. *71*, 1307–1318. https://doi.org/10.1107/S1399004715005945.

Yokoyama, H., Fujii, S., and Matsui, I. (2008). Crystal structure of a core domain of stomatin from *Pyrococcus horikoshii* Illustrates a novel trimeric and coiled-coil fold. J. Mol. Biol. *376*, 868–878. https://doi.org/10.1016/j.jmb.2007.12.024.

Yokoyama, T., Niinae, T., Tsumagari, K., Imami, K., Ishihama, Y., Hizukuri, Y., and Akiyama, Y. (2021). The *Escherichia coli* S2P intramembrane protease RseP regulates ferric citrate uptake by cleaving the sigma factor regulator FecR. J. Biol. Chem. *296*, 100673. https://doi.org/10.1016/j.jbc.2021.100673.

STAR★METHODS

KEY RESOURCES TABLE

REAGENT or RESOURCE	SOURCE	IDENTIFIER
Antibodies		
anti-Myc antibody	Santa Cruz Biotechnology	Cat# 9E10; RRID:AB_2857941
anti-FtsH antibody	(Kihara et al., 1996)	N.A
anti-HflKC	(Kihara et al., 1998)	N.A
Goat Anti-Rabbit IgG(H + L)-HRP Conjugate	Bio-Rad	Cat# 170-6515; RRID:AB_11125142
Goat Anti-Mouse IgG(H + L)-HRP Conjugate	Bio-Rad	Cat# 170-6516; RRID:AB_11125547
Bacterial and virus strains		
E. coli strains are listed in Table S4	This study	N/A
Chemicals, peptides, and recombinant proteins		
HEPES	Bio Basic	Cat# HB0264
Tris Base	Promega	Cat# H5133
Sodium Chloride	1st Base	Cat# 1111
Imidazole	Bio Basic	Cat# IB0277
Magnesium chloride	Sigma	Cat# M2670
Zinc chloride	Sigma	Cat# 96468
Sucrose	Sigma	Cat# S0389
Glutaraldehyde	Sigma	Cat# G5882
AMPPNP	Sigma	Cat# 10102547001
Nickel-NTA agarose	GE Healthcare	Cat# 17526802
Ampicillin Sodium	Goldbio	Cat# A-301-50
Kanamycin monosulfate	Goldbio	Cat# K-120-50
Amersham™ ECL™ Western Blotting Detection Reagents	Cytiva	Cat# RPN2106
Amersham™ Prime ECL™ Western Blotting Detection Reagents	Cytiva	Cat# RPN2236
PrimeSTAR MAX DNA Polymerase	Takara	Cat# R045A
isopropyl-β-D-thiogalactopyranoside (IPTG)	Wako	Cat# 097-05014
Adenosine-3′,5′-cyclic monophosphate Sodium Salt	Nacalai Tesque	Cat# 02289-16
Methionine, L-[^{35}S], translation grade	ARC	Cat# ARS0104A
Nonidet P-40, nuclease tested	Nacalai Tesque	Cat# 23640-65
Critical commercial assays		
ATPase/GTPase Activity Assay Kit	Sigma	Cat# MAK113
Universal Protease Substrate Kit	Roche	Cat# 11734334001
Deposited data		
FtsH-HflKC	This paper	EMD-32522
FtsH^{PD+TM}-HflKC	This paper	PDB: 7WI3; EMD-32520
FtsH^{PD+TM}	This paper	EMD-25233
FtsH	This paper	EMD-32524
FtsH^{CD}	This paper	PDB: 7WI4; EMD-32521
Recombinant DNA		
pRSFDuet-1-HflC-HflK	Novagen	pRSFDuet-1 Vector
pET-28a-FtsH	Novagen	pET-28a (+) Vector
Other plasmids are listed in Table S5	This study	N/A

(*Continued on next page*)

Continued

REAGENT or RESOURCE	SOURCE	IDENTIFIER
Software and algorithms		
SerialEM	(Mastronarde, 2005)	http://bio3d.colorado.edu/SerialEM/
Relion3.1	(Scheres, 2012)	https://www3.mrc-lmb.cam.ac.uk/relion/index.php/Main_Page
Phenix	(Adams et al., 2010)	https://www.phenix-online.org
PyMOL	(DeLano, 2002)	https://github.com/schrodinger/pymol-open-source
DeepEMhancer	(Sanchez-Garcia et al., 2021)	https://github.com/rsanchezgarc/deepEMhancer
UCSF Chimera	(Pettersen et al., 2004)	https://www.cgl.ucsf.edu/chimera/
UCSF Chimera X	(Pettersen et al., 2021)	https://www.cgl.ucsf.edu/chimerax/
COOT	(Emsley et al., 2010)	https://www2.mrc-lmb.cam.ac.uk/personal/pemsley/coot
GraphPad Prism	GraphPad Prism Software, Inc.	N/A
Multi Gauge	Cytiva	N/A
Other		
Quantifoil R 1.2/1.3 Au 400 Mesh	Electron Microscopy Sciences	Cat# Q4100AR1.3
Immobilon-P membrane filter	Merck Millipore	Cat# IPVH00010

RESOURCE AVAILABILITY

Lead contact

Further information and requests for resources and reagents should be directed to and will be fulfilled by the Lead Contact, Yong-Gui Gao (ygao@ntu.edu.sg).

Materials availability

All materials generated in this study will be made available on request by the Lead Contact.

Data and code availability

- Cryo-EM maps and atomic coordinates of $FtsH^{PD+TM}$-HflKC have been deposited in the EMDB and PDB under ID codes EMDB: EMD-32520 and PDB: 7WI3; Cryo-EM maps and atomic coordinates of $FtsH^{CD}$ have been deposited in the EMDB and PDB under ID codes EMDB: EMD-32521 and PDB: 7WI4. Cryo-EM maps of entire FtsH-HflKC, $FtsH^{PD+TM}$, and FtsH have been deposited in the EMDB under codes EMDB: EMD-32522, EMD-32523, and EMD-32524, respectively.
- This paper does not report original code.
- Any additional information required to reanalyze the data reported in this paper is available from the lead contact upon request.

EXPERIMENTAL MODEL AND SUBJECT DETAILS

The *Escherichia coli* strains used in the functional studies were *Escherichia coli* K12 derivatives (Table S4) (Akiyama et al., 1994; Kihara et al., 1995, 1998; Silhavy et al., 1984; Shimohata et al., 2002). The detailed information of *E. coli* strains used in this research are listed in Table S4. The cells were grown in M9-based medium at 37°C for the pulse-chase assay, or in LB medium (10 g/L Bacto tryptone, 5 g/L yeast extract, and 5 g/L NaCl; pH adjusted to 7.2 with NaOH) at 37°C for the immunoblotting and pull-down assay. *E. coli strain C41* was used for FtsH-HflKC protein complex expression and purification. The cells were cultured in 2xYT medium (16 g/L tryptone, 10 g/L yeast extract, and 5 g/L NaCl).

METHOD DETAILS

Cloning and site-directed mutagenesis

E. coli K12 strain full-length HflC (1–334) and HflK (1–419) were cloned into the pRSFDuet-1 vector, and the full-length FtsH was cloned into the pET28-a vector introducing a C-terminal non-cleavable hexahistidine tag. The constructs were verified by DNA sequencing. Mutagenesis was carried out using a quick-change mutagenesis kit. For *in vivo* assays, the plasmid pYK352 was constructed by replacing the codons for K61, D62, and S63 with an Ala codon (GCA, GCT, or GCT, respectively) in *ftsH-his*$_6$*-myc* on pSTD233 by site-directed mutagenesis. pYK354 and pYK357 were constructed by replacing the codons for D62 or Q45 with an

F62 (TTC) or A45 (GCG) codon, respectively, in *ftsH-his$_6$-myc* on pSTD233 by site-directed mutagenesis. The plasmid pHM1530 was constructed by cloning a NcoI/HindIII fragment of pNA3 (*secY-his$_6$-myc*) into a derivative of pSTV28 with a NcoI site at the *lacZ*α initiation codon. All plasmids used in this study were listed in Table S5 (Akiyama et al., 1998; Mori et al., 2003).

Media

L broth (10 g/L Bacto tryptone, 5 g/L yeast extract, and 5 g/L NaCl; pH adjusted to 7.2 with NaOH) and M9 medium (without $CaCl_2$) (Miller, 1972) supplemented with 2 μg/mL thiamine and 0.4% glucose were used for cultivation of *E. coli* cells. Ampicillin (50 μg/mL) and/or chloramphenicol (20 μg/mL) were added for selecting transformants and for growing plasmid-harboring cells. Bacterial growth was monitored using a miniphoto 518R (660 nm; TAITEC) device or Klett-Summerson colorimeter (filter No. 54; Klett Manufacturing).

Immunoblotting

Cells were grown, and the total cellular proteins were precipitated with 5% trichloroacetic acid, washed with acetone, and dissolved in SDS sample buffer. Immunoblotting was carried out essentially as described previously (Yokoyama et al., 2021). Proteins were separated by SDS–PAGE and electroblotted onto an Immobilon-P membrane filter (Millipore Sigma). After blocking, the filter was incubated with an appropriate antibody. Monoclonal anti-Myc antibody (c-Myc (9E10), Santa Cruz Biotechnology), rabbit polyclonal anti-FtsH antibody (Kihara et al., 1996), and anti-HflKC antibody (Kihara et al., 1998) were used for immunoblotting. For anti-HflKC immunoblotting, anti-HflKC antibodies were preincubated with whole-cell lysates of AK1136 (the Δ*hflKC* strain) at 4°C for 1 h to reduce the background. The filter was then washed and incubated with goat anti-mouse or anti-rabbit IgG conjugated with horseradish peroxide (Bio–Rad). After washing the filter, proteins that reacted with secondary antibodies were visualized using ECL or ECL Prime Western blotting Detection Reagents (Cytiva) and a mini LAS4000 Bio image analyzer (Cytiva) or an LAS3000 (Cytiva) instrument.

Pulse-chase experiment

Pulse-chase analysis of CII degradation was conducted according to a procedure described previously (Akiyama et al., 1998). The cells were grown at 37°C in M9-based medium for 1.5 h until the early log phase, induced with 1 mM IPTG and 1 mM cAMP for 1 h, and then pulse labeled with [^{35}S] methionine for 30 s, followed by chasing with an excess amount of unlabeled methionine for 0.5/5/10/20/40 min. The proteins of a fixed total radioactivity were separated by the modified Laemmli system with 15% polyacrylamide and 0.12% N,N′-methylene-bis-acrylamide gel and visualized for quantification using phosphor imager BAS5000 (Cytiva). Intensities associated with the CII bands were determined and normalized to the value for 30 s chase sample.

Pull-down assay

AD1691 cells (the background of this strain is AD16) expressing FtsH-His$_6$-Myc or its mutants were harvested, washed with 10 mM Tris-HCl (pH 8.1), and resuspended in 20% sucrose and 30 mM Tris-HCl (pH 8.1), followed by the addition of 1/10 volume of 1 g/L lysozyme dissolved in 0.1 M EDTA (pH 7.0) and incubated for 1 h on ice. Centrifugation at 26,000 × *g* for 10 min yielded supernatants and pellets. The cells of AD16 derivatives were lysed by this treatment, and the pellets contained crude membranes (Akiyama and Ito, 1985; Shimoike et al., 1995). The pellets were solubilized by incubation in buffer A (50 mM Tris-HCl (pH 8.1), 200 mM KCl, 10 mM imidazole, 10% glycerol, 0.5% Nonidet P-40, and 10 mM 2-mercaptoethanol) at 4°C for 1 h with rotation. After removal of insoluble materials by centrifugation, proteins were incubated with Ni-NTA agarose (Qiagen) at 4°C for 1 h with rotation, washed twice with buffer B (10 mM Tris-HCl (pH 8.1), 500 mM KCl, 20 mM imidazole, 10% glycerol, and 0.5% Nonidet P-40) and eluted with buffer C (50 mM Tris-HCl (pH 8.1), 300 mM KCl, 500 mM imidazole, 10% glycerol, 0.5% Nonidet P-40, and 10 mM 2-mercaptoethanol). All the fractions were mixed with 1/5 volume of 5x SDS sample buffer (312.5 mM Tris-HCl (pH 6.8), 10% (w/v) SDS, 50% glycerol, and trace of bromophenol blue) and 1/10 volume of 2-mercaptoethanol to yield SDS–PAGE samples.

Protein expression and purification

The two plasmids pRSFDuet-1-HflC-HflK and pOPT-Chis-FtsH were cotransformed into *E. coli* C41 for protein expression. A single colony was selected and cultured in 2xYT media, and protein expression was induced by adding a final concentration of 0.2 mM IPTG. Bacteria were grown at 37°C for 4 h. Cells were harvested by centrifugation at 4,000 × g for 10 min. The cell pellet was resuspended in buffer (20 mM Tris (pH 7.5) and 150 mM NaCl). Bacteria were lysed by sonication and centrifuged at 10,000 × g for 10 min to remove the cell debris as well as the unbroken cells. The supernatant was loaded for ultracentrifugation at 150, 000 x g (Beckman, USA, Ti45) for 40 min. The membrane was resuspended in buffer (20 mM Tris (pH 7.5), 150 mM NaCl, 10% glycerol, and 1% DDM) and incubated in a cold room for 1 h. Then, the solubilized membrane protein was collected via centrifugation at 150, 000 x g (Beckman, USA, Ti45) for 30 min. The supernatant was collected and incubated with preequilibrated nickel-NTA beads in a cold room for 1 h. The FtsH-HflKC complex was purified by gravity column after extensive washing and subsequent elution with 20 mM Tris (pH 7.5), 150 mM NaCl, 0.02% GDN, and 200 mM imidazole. The FtsH-HflKC complex was concentrated using a 100 kDa cutoff MWCO concentrator (Millipore) and loaded onto a Superose 6 10/30 gel filtration column (GE Healthcare) preequilibrated with buffer (20 mM HEPES (pH 7.5), 150 mM NaCl, and 0.02% GDN). The fractions containing the target proteins were pooled and concentrated to 2 mg/mL.

Crosslinking of the FtsH-HflKC complex

For the Grafix gradient (Kastner et al., 2008), two buffer solutions were prepared separately based on the buffer (20 mM HEPES, pH 7.5, 100 mM NaCl, and 0.02% GDN): the top buffer contained 15% sucrose, and the bottom buffer contained 45% sucrose as well as 0.1% glutaraldehyde (GA). First, 2.2 mL of top solution was added to a 4.4 mL centrifuge tube (Beckman, USA), and the bottom solution was carefully injected by a blunt-end syringe into the bottom of the centrifuge tube. A continuous gradient was formed by executing the standard 15–45% sucrose gradient program in Gradient Master 108 (Biocomp). The gradients were cooled to 4°C, 100 μL of FtsH-HflKC complex (1 mg/mL) was loaded on the top of the gradient and then subjected to ultracentrifugation at 100, 000 x g (SW60, Beckman, USA) for 16 h at 4°C. Following ultracentrifugation, a peristaltic pump was used at 4°C for fractionation starting from the bottom of the tube with three drops per fraction. All fractions were subjected to SDS–PAGE analysis.

In vitro ATPase and protease assays of the FtsH-HflKC complex

ATPase activities were measured using the ATPase/GTPase Activity Assay Kit (MAK-113, Sigma–Aldrich) according to the manufacturer's instructions. Briefly, purified FtsH-HflKC was diluted to 0.1 to 0.5 μmol/L with assay buffer (20 mM HEPES (pH 7.5), 150 mM NaCl, 5 mM $MgCl_2$, and 0.02% GDN) with a final concentration of 0.2 mM ATP. Then, 20 μL of the reaction mixture containing the diluted protein was incubated for 30 min at room temperature. Then, 100 μL of malachite green reagent was added to each reaction well and incubated for 30 min. Triplicate measurements were carried out. Afterward, the absorbance at 620 nm was measured, which is proportional to the enzyme activity present. FtsH-HflKC protease activity was assessed using a resorufin-labeled casein kit (Sigma–Aldrich). FtsH-HflKC (0.5 μM) was incubated with 50 μM resorufin-labeled casein in (20 mM HEPES (pH 7.5), 150 mM NaCl, 5 mM $MgCl_2$, 50 μM $ZnCl_2$ 0.02% GDN, and 2 mM ATP) at 37°C. Triplicate measurements were carried out. The reaction rates were measured at 5 min, 10 min, 15 min, and 30 min. Then, 50 μL of 5% trichloroacetic acid was added and incubated at 37°C for 10 min. Proteins were precipitated at 20,000 × *g* for 10 min, and 60 μL from the supernatant was mixed with 30 μL of 1.5 M Tris-HCl (pH 8.8) and then added to a 96-well transparent plate. The OD_{574nm} was immediately measured using a plate reader (TECAN).

Negative staining electron microscopy

Suitable fractions from Grafix were diluted 3 times in buffer: 20 mM HEPES pH 7.5, 100 mM NaCl, and 0.02% GDN. Continuous carbon film-coated 200-mesh copper grids (Electron Microscopy Sciences, CF200-CU) were glow discharged for 35 s, and 4 μL of protein at a concentration of 0.04 mg/mL was applied to the grids. After 1 min of incubation, the protein was blotted away by filter paper (Whatman). Then, 4 μL of 2% uranyl acetate was immediately added to the grid, incubated for 1 min, and gently blotted away with filter paper. The grids were air-dried for 10 min before they were loaded into an FEI Tecnai T12 instrument equipped with a 4K Eagle charge-coupled device (CCD) camera. Images were collected at 49,000 nominal magnifications with a pixel size of 2.11 Å/pixel. Micrographs were collected at an electron dose of approximately 20 $e-/Å^2$.

Cryo-EM

Suitable fractions from Grafix were collected, and the buffer was exchanged to final buffer (20 mM HEPES (pH 7.5), 100 mM NaCl, and 0.02% GDN) by a 5 mL HiTrap Desalting column (GE Healthcare) to remove the sucrose. The Quantifoil AU 1.2/1.3 grids coated with graphene were glow-discharged for 10 s before mounting to Vitrobot tweezers. The blotting was performed at 4°C with 100% humidity. The blotting protocol was as follows: 1 s blot time, 1 blot force, 10 s waiting time, 1 blot total, and 0 s drain time. A total of 4 μL of protein sample at a concentration of 0.6 mg/mL was applied to the cryo-EM grids, immersed into a liquid ethane container and carefully transferred to a grid box in liquid nitrogen. The datasets were collected on a Titan Krios (Thermo Fisher Scientific, USA) 300 kV electron microscope equipped with a GIF Quantum energy filter and a K3 direct electron detector (Gatan, USA) with a defocus range between −1 and −2 μm under superresolution mode with a pixel size of 0.428 Å by SerialEM (Mastronarde, 2005). Movies were acquired via SerialEM employing a 9-hole beam-image shift acquisition mode in 50 frames.

Micrographs were imported to Relion 3.1 for beam-induced motion correction by MotionCor 2.1 (Scheres, 2012). CTFFind 4.1 was used to estimate the contrast transfer function (CTF) parameters (Rohou and Grigorieff, 2015). Micrographs with estimated resolution higher than 6 Å were selected for subsequent processing. Particles were autopicked via the Laplacian of Gaussian method in Relion 3.1 and extracted with box size 128 and pixel size 3.432 Å. All the extracted particles were subjected to 2 rounds of reference-free 2D classification. The good classes with clear protein feathers were selected and used for initial model building and two rounds of 3D classification. Only the models that clearly showed four FtsH hexamers were selected as good particles and reextracted to box size 320 and pixel size 1.372 Å. The reextracted particles were used for 3D-autorefine and resulted in the construction of an ~7 Å map. Since the FtsH-HflKC complex is too dynamic, subregion subtraction and focused 3D classification were used to improve the subregion resolution. Based on consensus refinement, the entire periplasm and transmembrane region ($FtsH^{PD+TM}$-HflKC), the FtsH full-length hexamer, FtsH hexamer without the cytosolic domain ($FtsH^{PD+TM}$), and FtsH cytosolic domain hexamer ($FtsH^{CD}$), were extracted individually and subjected to focused 3-D classification, autorefinement, and CTF refinement. Soft masks were generated in Relion 3.1 accordingly. The resolutions of the resulting maps for $FtsH^{PD+TM}$-HflKC, full-length FtsH, $FtsH^{PD+TM}$, and $FtsH^{CD}$ reached 4.0 Å, 6.1 Å, 6.5 Å, and 3.3 Å, respectively, with symmetry (C4, C1, C1, and C6) imposed, respectively. The resolution estimations were based on gold-standard Fourier shell correlation (FSC) = 0.143 criterion in Relion 3.1. The reconstructed EM maps

were density-modified by DeepEMhancer for illustration purpose (Sanchez-Garcia et al., 2021). The FtsH^{PD+TM}-HflKC map was used for *ab initio* model building in Phenix Suite (Adams et al., 2010). The crystal structure of *E. coli* FtsH^{PD} (PDB ID: 4V0B) was manually fitted into the FtsH^{PD+TM}-HflKC map. The crystal structure of *Thermotoga maritima* FtsH (PDB ID: 3KDS) was used as the initial model and later manually corrected to the FtsH^{CD} map to obtain the FtsH^{CD} model. The predicted FtsH^{TM} hexamer from Alphafold 2 was manually fitted to the FtsH^{PD+TM} map (Jumper et al., 2021). Models of FtsH^{PD+TM}-HflKC and FtsH^{CD} were subjected to the Phenix real-space refinement and manually adjusted by COOT (Adams et al., 2010; Emsley et al., 2010). All the structure-related figures and movies were prepared by PyMol, Chimera, and ChimeraX (DeLano, 2002; Pettersen et al., 2004, 2021).